# Phonons and lattice dielectric properties of zirconia

Xinyuan Zhao and David Vanderbilt
*Department of Physics and Astronomy, Rutgers University, Piscataway, New Jersey 08854-8019*
(Received 29 August 2001; published 18 January 2002)

We have performed a first-principles study of the structural and vibrational properties of the three low-pressure (cubic, tetragonal, and especially monoclinic) phases of $ZrO_2$, with special attention to the computation of the zone-center phonon modes and related dielectric properties. The calculations have been carried out within the local-density approximation using ultrasoft pseudopotentials and a plane-wave basis. The fully relaxed structural parameters are found to be in excellent agreement with experimental data and with previous theoretical work. The total-energy calculations correctly reproduce the energetics of the $ZrO_2$ phases, and the calculated zone-center phonon frequencies yield good agreement with the infrared and Raman experimental frequencies in the monoclinic phase. The Born effective charge tensors are computed and, together with the mode eigenvectors, used to decompose the lattice dielectric susceptibility tensor into contributions arising from individual infrared-active phonon modes. This work has been partially motivated by the potential for $ZrO_2$ to replace $SiO_2$ as the gate-dielectric material in modern integrated-circuit technology.

DOI: 10.1103/PhysRevB.65.075105 PACS number(s): 77.22.−d, 61.66.−f, 63.20.−e, 77.84.Bw

## I. INTRODUCTION

$ZrO_2$, or zirconia, has a wide range of materials applications because of its high strength and stability at high temperature. A prospective application of particular current interest is its possible use to replace $SiO_2$ as the gate-dielectric material in metal-oxide-semiconductor (MOS) devices.

The use of $SiO_2$ as the gate dielectric and, in particular, the quality of the $Si/SiO_2$ interface have been a foundation of modern integrated-circuit technology since its invention decades ago. Driven by the seemingly endless pressure for higher operation speed, smaller physical dimensions, and lower driving voltage, the gate dielectric thickness in integrated circuits has been rapidly reduced from the order of $1-2\ \mu$m in the early 1960s to the current value of about $2-3$ nm. If $SiO_2$ is not replaced by another material, this would require the gate-dielectric thickness to be reduced to less than 1 nm in the coming decade.[1] Such a reduction in gate oxide thickness, however, would impose several severe problems on the current $Si/SiO_2$ semiconductor technology, including a high level of direct tunneling current, a large degree of dopant (boron) diffusion in the gate oxide, and reliability problems associated with nonuniformity of the very thin film. It has been demonstrated that the direct tunneling current grows exponentially as the thickness of the gate dielectric film decreases.[2,3] For films thinner than 2 nm, the tunneling current could become as large as 1 $A/cm^2$, which would require a level of power dissipation that would be intolerable for most digital device applications.[4] These fundamental problems are largely attributable to the inherently low dielectric constant of silicon dioxide ($\epsilon \simeq 3.5$), quite small in comparison with many other oxide dielectrics.

Several approaches have been proposed for overcoming these fundamental challenges associated with the use of $SiO_2$ films. In particular, much recent effort has been focused on metal oxides having a larger dielectric constant than that of $SiO_2$, since these might be used to provide physically thicker dielectric films that are equivalent to much thinner $SiO_2$ ones in terms of their capacitance, but exhibiting a greatly reduced leakage current. Some of the proposed candidates include $Ta_2O_5$,[5,6] $TiO_2$, $ZrO_2$, $Y_2O_3$, $Al_2O_3$, and hafnium and zirconium silicate systems ($Hf_{1-x}Si_xO_2$ and $Zr_{1-x}Si_xO_2$).[7] Among these candidates, $ZrO_2$ is a promising one because of its good dielectric properties ($\epsilon \sim 20$) and thermodynamic stability in contact with the Si substrate.

Zirconia is known to have three low-pressure structural phases. The system passes from the monoclinic ground state to a tetragonal phase, and then eventually to a cubic phase, with increasing temperature. The monoclinic phase (space group $C_{2h}^5$ or $P2_1/c$) is thermodynamically stable below 1400 K. Around 1400 K a transition occurs to the tetragonal structure (space group $D_{4h}^{15}$ or $P4_2/nmc$), which is a slightly distorted version of the cubic structure and is stable up to 2570 K. Finally, the cubic phase (space group $O_h^5$ or $Fm3m$) is thermodynamically stable between 2570 K and the melting temperature at 2980 K. This information is summarized in Table I, which also shows the coordination number of the Zr and O atoms for each of the three phases. In the monoclinic phase there are two nonequivalent oxygen sites with coordination numbers of 3 ($O_1$) and 4 ($O_2$), while all the Zr atoms are equivalent and have a coordination of 7.

Our purpose is to investigate the lattice contributions to the dielectric properties of these three $ZrO_2$ phases, especially the monoclinic phase. Because previous experimental and theoretical work indicates that the electronic contribution

TABLE I. The three low-pressure phases of $ZrO_2$. The last three columns give the coordination numbers of the Zr and O atoms. (Atoms $O_1$ and $O_2$ are equivalent in the cubic and tetragonal, but not in the monoclinic, structures.)

| Phase | Space group | $T$ (K) | Coordination Zr | $O_1$ | $O_2$ |
|---|---|---|---|---|---|
| Cubic | $Fm3m$ | 2570–2980 | 8 | 4 | 4 |
| Tetragonal | $P4_2/nmc$ | 1400–2570 | 8 | 4 | 4 |
| Monoclinic | $P2_1/c$ | $<1400$ | 7 | 3 | 4 |

 

to the dielectric constant is rather small ($\epsilon_\infty \simeq 5$) and is neither strongly anisotropic nor strongly dependent on structural phase[8–12] and because $\epsilon_\infty$ is best calculated by specialized linear-response techniques, we have not calculated it here. Instead, we focus on the lattice contributions to the dielectric response because, as we shall see, these are much larger, more anisotropic, and more sensitive to the lattice structure.

In order to achieve this, the Born effective charge tensors and the force-constant matrices are calculated for the three $ZrO_2$ phases using density-functional theory. We first check that our relaxed structural parameters and energy differences between phases are consistent with previous theoretical[13–20] and experimental work.[21,22] The Born effective charge tensors are then computed from finite differences of polarizations as various sublattice displacements are imposed, with the polarizations computed using the Berry-phase method.[23] The force constants are obtained in a similar way from finite differences of forces. Reasonable agreement is found between the calculated frequencies and the measured spectra for both IR-active and Raman-active modes,[9,24–27] although possible reassignments are proposed for certain modes based on the results of our calculations. Finally, our theoretical information is combined to predict the lattice contributions to the bulk dielectric tensor. We thus clarify the dependence of the dielectric response on crystal phase, orientation, and lattice dynamical properties. In particular, we find that the lattice dielectric tensors in the tetragonal and monoclinic phases are strongly anisotropic. We also find that the monoclinic phase has the smallest orientationally averaged dielectric constant of the three phases, owing to the fact that the mode effective charges associated with the lowest-frequency modes are rather weak.

The paper is organized as follows. In Sec. II we briefly describe the technical aspects of our first-principles calculations. Section III presents the results, including the structural relaxations, the Born effective charge tensors, the phonon normal modes, and the lattice contributions to the dielectric tensors. Section IV concludes the paper.

## II. DETAILS OF FIRST-PRINCIPLES CALCULATIONS

The calculations are carried out within a plane-wave pseudopotential implementation of density-functional theory (DFT) in the local-density approximation (LDA) using Ceperley-Alder exchange correlation.[28,29] The use of Vanderbilt ultrasoft pseudopotentials[30] allows highly accurate calculations to be achieved with a low-energy cutoff, which is chosen to be 25 Ry in this work. The $4s$ and $4p$ semicore shells are included in the valence for Zr, and the $2s$ and $2p$ shells are included in the valence for O. A conjugate-gradient algorithm is used to compute the total energies and forces. For each of the three $ZrO_2$ phases, a unit cell containing 12 atoms (4 Zr and 8 O atoms) is used in our calculations. Although we thus use an unnecessarily large cell for the cubic and tetragonal phases, this approach has the advantage that the three zirconia phases can be studied in a completely parallel fashion.

A $4\times4\times4$ Monkhorst-Pack[31] **k**-point mesh is found to provide sufficient precision in the calculations of total energies and forces. In order to calculate Born effective charges and force-constant matrices, each atomic sublattice in turn is displaced in each Cartesian direction by $\pm 0.2\%$ in lattice units, and the Berry-phase polarization[23] and Hellmann-Feynman forces are computed. To be specific, a $4\times4\times20$ **k**-point sampling over the Brillouin zone was used in the Berry-phase polarization calculations, and we have confirmed that good convergence was achieved for the three $ZrO_2$ phases with such **k**-point sampling. The Born effective charge tensors and force-constant matrices are then constructed by finite differences from the results of these calculations.

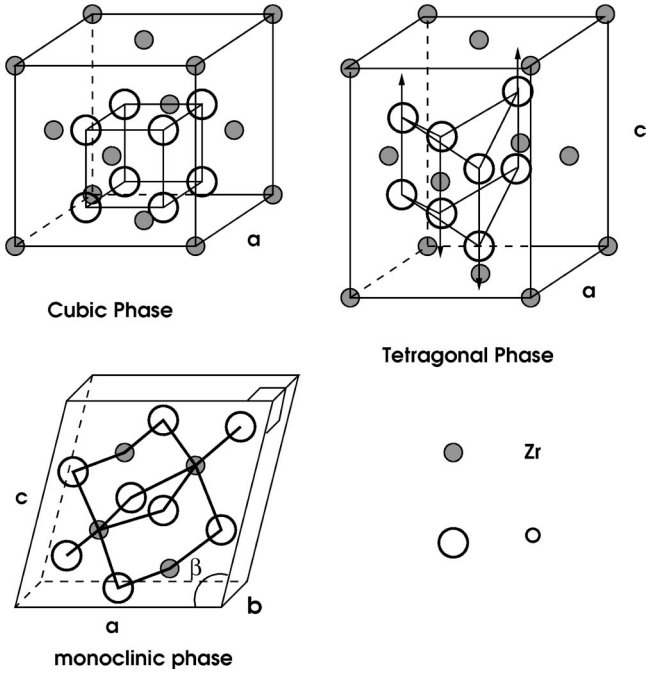


FIG. 1. Structures of the three $ZrO_2$ phases. The Zr-O bonds are only shown in the monoclinic structure. For the tetragonal phase, the arrows indicate the distortion of oxygen pairs relative to the cubic structure.

## III. RESULTS

### A. Atomic structures of $ZrO_2$ phases

The three crystal structures of $ZrO_2$ are shown in Fig. 1. Cubic zirconia takes the fluorite ($CaF_2$) structure, in which the Zr atoms are in a face-centered-cubic structure and the oxygen atoms occupy the tetrahedral interstitial sites associated with this fcc lattice. The structure of tetragonal zirconia can be regarded as a distortion of the cubic structure obtained by displacing alternating pairs of oxygen atoms up and down by an amount $\Delta z$ along the $z$ direction, as shown in the figure. This doubles the primitive cell from three to six atoms and is accompanied by a tetragonal strain. The structure can be specified by the two lattice parameters $a$ and $c$ and a dimensionless ratio $d_z = \Delta z/c$. Cubic zirconia can be considered as a special case of the tetragonal structure with $d_z = 0$ and $c/a = 1$ (if the primitive cell is used for tetragonal phase, $c/a = \sqrt{2}$).

TABLE II. Structural parameters obtained for three $ZrO_2$ phases from present theory, compared with previous pseudopotential (PP) and linear augmented plane-wave (FLAPW) calculations and with experiment. Lattice parameters *a*, *b*, *c* and volume per formula unit *V* are in atomic units; monoclinic angle $\beta$ is in degrees; and internal coordinates $d_z$, *x*, *y*, and *z* are dimensionless.

| | This work | PP[a] | FLAPW[b] | Expt.[c] |
|---|---|---|---|---|
| Cubic | | | | |
| *V* | 215.612 | 215.31 | 217.79 | 222.48 |
| *a* | 9.5187 | 9.514 | 9.551 | 9.619 |
| Tetragonal | | | | |
| *V* | 217.698 | 218.69 | 218.77 | 222.96 |
| *a* | 9.5051 | 9.523 | 9.541 | 9.543 |
| *c* | 9.6383 | 9.646 | 9.613 | 9.793 |
| $d_z$ | 0.0418 | 0.0423 | 0.029 | 0.0574 |
| Monoclinic | | | | |
| *V* | 231.822 | 230.51 | | 237.71 |
| *a* | 9.6532 | 9.611 | | 9.734 |
| *b* | 9.7690 | 9.841 | | 9.849 |
| *c* | 9.9621 | 9.876 | | 10.048 |
| $\beta$ | 99.21 | 99.21 | | 99.23 |
| $x_{Zr}$ | 0.2769 | 0.2779 | | 0.2754 |
| $y_{Zr}$ | 0.0422 | 0.0418 | | 0.0395 |
| $z_{Zr}$ | 0.2097 | 0.2099 | | 0.2083 |
| $x_{O_1}$ | 0.0689 | 0.0766 | | 0.0700 |
| $y_{O_1}$ | 0.3333 | 0.3488 | | 0.3317 |
| $z_{O_1}$ | 0.3445 | 0.3311 | | 0.3447 |
| $x_{O_2}$ | 0.4495 | 0.4471 | | 0.4496 |
| $y_{O_2}$ | 0.7573 | 0.7588 | | 0.7569 |
| $z_{O_2}$ | 0.4798 | 0.4830 | | 0.4792 |

[a]Reference 16.
[b]Reference 20.
[c]Reference 13.

Monoclinic zirconia has a lower symmetry and a more complex geometric structure with a 12-atom primitive cell. The lattice parameters are *a*, *b*, *c*, and $\beta$ (the nonorthogonal angle between **a** and **c**) as shown in Fig. 1. The atomic coordinates in Wyckoff (lattice-vector) notation are $\pm(x,y,z)$ and $\pm(-x,y+1/2,1/2-z)$, with parameters *x*, *y*, and *z* specified for each of three kinds of atoms: Zr, $O_1$, and $O_2$. Note that there are two nonequivalent oxygen sites: atoms of type $O_1$ are threefold coordinated, while $O_2$ are fourfold coordinated. All Zr atoms are equivalent and are sevenfold coordinated. Thus, four lattice-vector parameters and nine internal parameters are needed to specify the structure fully.

Tabulated in Table II are the relaxed structural parameters for the three phases of $ZrO_2$ as computed within our energy minimization procedure, as well as results of previous theoretical and experimental work for comparison. Figure 2 illustrates the relaxed structure for the monoclinic phase. The origin and orientation of the unit cell in Fig. 2 are carefully chosen in such a way that the geometry of the atoms, labeled as Zr, $O_1$, and $O_2$ in Fig. 2, corresponds precisely with the

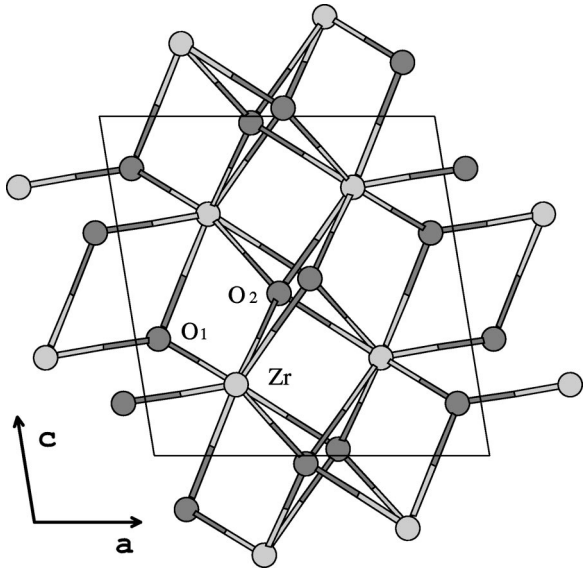


FIG. 2. Relaxed lattice structure of monoclinic $ZrO_2$; the unit cell is outlined. Light and dark circles stand for the Zr and O atoms, respectively. A threefold-coordinated oxygen atom ($O_1$) is bonded to the nearest-neighboring Zr atoms in an almost planar configuration, while a fourfold oxygen ($O_2$) forms a distorted tetrahedron with the Zr neighbors.

parameters given in Table II. The experimental parameters given in the last column were used as the starting point for our DFT-LDA structural relaxations. It can readily be seen that there is excellent agreement between our results and previous theory and experiment. The volumes are all slightly underestimated, by 2%–3%, as is typical of LDA calculations. The largest discrepancy is for $d_z=\Delta z/c$, the internal coordinate in the tetragonal phase; our value is $\sim$30% smaller than the experimental value, but it is very close to the results of the previous pseudopotential calculation. (The discrepancy with experiment should not be taken too seriously, in view of the fact that the theory is a zero-temperature one.) The very close (usually $<1\%$) agreement with the previous pseudopotential results of Ref. 16 provides a good confirmation of the reliability of our calculations.

Table III lists the calculated bond lengths and bond angles for the O-Zr bonds. Bond lengths taken from Ref. 32 are also listed for comparison. A threefold-coordinated oxygen atom (e.g., $O_1$ in Fig. 2) is bonded to the three nearest-neighbor Zr atoms in an almost planar configuration, as can be verified by noting that the sum of the three bond angles is about 350°. A second fourfold oxygen atom (e.g., $O_2$ in Fig. 2) forms a distorted tetrahedron with its four nearest Zr neighbors, the degree of distortion being evident from the lengths and angles in the table. The presence of these two distinct oxygen atoms with utterly different environments suggests that their contributions to the dielectric properties of the material may be quite different. We shall see how this is manifest as a difference of the Born effective charge tensors for $O_1$ and $O_2$ in the next subsection.

Our total-energy calculations have correctly reproduced the energetics of the three $ZrO_2$ phases. The differences of total energies per formula unit for the monoclinic and tetrag-

TABLE III. O-Zr bond lengths and Zr-O-Zr bond angles in monoclinic zirconia (in Å and degrees, respectively). Values in parentheses are from Ref. 32 for comparison.

| | | | | |
|---|---|---|---|---|
| $O_1$-Zr bond lengths and angles | | | | |
| $d_1$ | 2.035 | (2.051) | $\theta_{12}$ | 138.6 |
| $d_2$ | 2.051 | (2.057) | $\theta_{13}$ | 106.3 |
| $d_3$ | 2.144 | (2.151) | $\theta_{23}$ | 105.0 |
| $O_2$-Zr bond lengths and angles | | | | |
| $d_1$ | 2.138 | (2.163) | $\theta_{12}$ | 108.6 |
| $d_2$ | 2.229 | (2.220) | $\theta_{13}$ | 106.0 |
| $d_3$ | 2.153 | (2.189) | $\theta_{14}$ | 133.0 |
| $d_4$ | 2.233 | (2.285) | $\theta_{23}$ | 102.0 |
| | | | $\theta_{24}$ | 100.6 |
| | | | $\theta_{34}$ | 103.6 |

onal phases, relative to the cubic phase, are 0.044 eV and 0.089 eV, respectively, to be compared with 0.045 eV and 0.102 eV from previous calculation[16] and 0.057 eV and 0.120 eV from one experiment.[33]

### B. Born effective charge tensors

The Born effective charge tensor quantifies the macroscopic electric response of a crystal to internal displacements of its atoms. We begin with a calculation of the bulk polarization **P**, using the Berry-phase polarization method to compute the electronic contribution, as formulated in Ref. 23. $\mathbf{Z}_i^*$, the Born effective charge tensor for the $i$th atom in the unit cell, is defined via

$$\Delta\mathbf{P}=\frac{e}{V}\sum_{i=1}^{N}\mathbf{Z}_i^*\cdot\Delta\mathbf{u}_i \tag{1}$$

where $V$ is the volume of the unit cell, $\Delta\mathbf{u}_i$ is the displacement of the $i$th atom in the unit cell, and $\Delta\mathbf{P}$ is the induced change in bulk polarization resulting from this displacement. Using Eq. (1), $\mathbf{Z}^*$ can be computed from finite differences of **P** under small but finite distortions.[34]

In the Berry-phase polarization scheme, one samples the Brillouin zone by a set of strings of **k** points set up parallel to some chosen reciprocal lattice vector, thereby computing the electronic polarization along that direction. For cubic and tetragonal $ZrO_2$, this is relatively straightforward since the reciprocal lattice vectors are all mutually perpendicular. For monoclinic $ZrO_2$, however, one has to transform the polarization to Cartesian coordinates after first computing it in lattice coordinates.

Our results for the dynamical effective charges of the three phases are presented in Table IV. In the cubic phase, symmetry requires that the Born effective charge tensor should be isotropic ($Z_{ij}^*=Z^*\,\delta_{ij}$) on each atom and that $Z^*(O_1)=Z^*(O_2)$; the neutrality sum rule requires that

TABLE IV. Born effective charges for three phases of $ZrO_2$. In the cubic phase, the $\mathbf{Z}^*$ tensors are diagonal and isotropic. In the tetragonal phase, the $\mathbf{Z}^*$ tensors are diagonal in an $x'$-$y'$-$z$ frame rotated 45° about $\hat{z}$ from the Cartesian frame; $Z_j^*$ ($j=1,2,3$) are $Z_{x'x'}^*$, $Z_{y'y'}^*$, and $Z_{zz}^*$, respectively. In the monoclinic phase, $Z_j^*$ is the $j$th eigenvalue of the symmetric part of the $\mathbf{Z}^*$ tensor.

| Phase | Atom | $Z_1^*$ | $Z_2^*$ | $Z_3^*$ |
|---|---|---|---|---|
| Cubic | Zr | 5.72 | 5.72 | 5.72 |
| | O | −2.86 | −2.86 | −2.86 |
| Tetragonal | Zr | 5.75 | 5.75 | 5.09 |
| | $O_1$ | −3.53 | −2.22 | −2.53 |
| | $O_2$ | −2.22 | −3.53 | −2.56 |
| Monoclinic | Zr | 4.73 | 5.42 | 5.85 |
| | $O_1$ | −4.26 | −2.64 | −1.19 |
| | $O_2$ | −3.20 | −2.52 | −2.26 |

$Z^*(\mathrm{Zr})=-2Z^*(\mathrm{O})$. The values given in Table IV can be seen to be in excellent agreement with the corresponding values of $Z^*(\mathrm{Zr})=5.75$ and $Z^*(\mathrm{O})=-2.86$ reported in Ref. 8.

In the tetragonal phase, $\mathbf{Z}^*(\mathrm{Zr})$ is diagonal in the Cartesian frame with $Z_{xx}^*=Z_{yy}^*\neq Z_{zz}^*$. The diagonal elements of $\mathbf{Z}^*(\mathrm{O})$ have the same form, but the shifting of oxygen atom pairs creates two different configurations for oxygen atoms (denoted $O_1$ and $O_2$) and introduces off-diagonal $xy$ elements. Specifically, $Z_{xy}^*(O_1)=Z_{yx}^*(O_1)=-Z_{xy}^*(O_2)=-Z_{yx}^*(O_2)$. Thus, it is more natural to refer to a reference frame that has been rotated 45° about the $\hat{z}$ axis; in this frame the $\mathbf{Z}^*(\mathrm{O})$ become diagonal. This symmetry analysis is confirmed in our calculations, as can be seen from Table IV. We have recently become aware of the independent work of Ref. 12, which also reports values for the $\mathbf{Z}^*$ tensors in the tetragonal phase of $ZrO_2$. These authors find $Z_{xx}^*=5.74$ and $Z_{zz}^*=5.15$ for Zr and $Z_{x'x'}^*=-3.52$, $Z_{y'y'}^*=-2.49$, and $Z_{zz}^*=-2.57$ for oxygens. Evidently there is again very good agreement between our results and those of previous theory.

In the monoclinic phase, the Born effective charge tensors are more complicated because of the complexity of the lattice structure. The two oxygen sites are now nonequivalent, and the crystal structure should be regarded as composed of three kinds of atoms, namely, Zr, $O_1$, and $O_2$. Each kind of atom appears four times in the unit cell, once at a ''representative'' Wyckoff position $(x,y,z)$, and then also at partner positions $(-x,-y,-z)$, $(-x,0.5+y,0.5-z)$, and $(x,0.5-y,0.5+z)$ given by action of the space-group operations $E$, $I$, $\{C_2^y\,|\,0,0.5,0.5\}$, and $\{M_y\,|\,0,0.5,0.5\}$. Thus, all three kinds of atoms have equally low symmetry, and their resulting $\mathbf{Z}^*$ tensors are neither diagonal nor symmetric. Specifically, for these representative atoms we find

$$Z^*(\mathrm{Zr})=\begin{pmatrix} 5.471 & -0.432 & 0.180 \\ -0.155 & 5.608 & 0.152 \\ 0.197 & 0.376 & 4.952 \end{pmatrix},$$

$$Z^*(\mathrm{O}_1)=\begin{pmatrix} -3.019 & 1.172 & -0.199 \\ 1.449 & -2.755 & -0.695 \\ -0.191 & -0.684 & -2.321 \end{pmatrix},$$

$$Z^*(\mathrm{O}_2)=\begin{pmatrix} -2.461 & 0.171 & 0.018 \\ 0.238 & -2.850 & 0.372 \\ -0.019 & 0.413 & -2.657 \end{pmatrix}.$$

We have confirmed that our computed effective-charge tensors for the other atoms obey the relations expected by symmetry, namely, that the $\mathbf{Z}^*$ tensors should be identical for partners at $(-x,-y,-z)$, and that the off-diagonal $xy$, $yx$, $yz$, and $zy$ matrix elements should change sign for the partners at $(-x,0.5+y,0.5-z)$ and $(x,0.5-y,0.5+z)$. In Table IV we report the eigenvalues of the symmetric part of the effective-charge tensors.

It is obvious from Table IV that the $Z^*$ values are quite different from the nominal ionic valences ($+4$ for Zr and $-2$ for O). Except for the value of $-1.19$, all other magnitudes are greater than their nominal valences. The anomalously large $Z^*$ values indicate that there is a strong dynamic charge transfer along the Zr-O bond as the bond length varies, indicating a mixed ionic-covalent nature of the Zr-O bond. Such an anomaly reflects the relatively delocalized structure of the electronic charge distributions and is quite common in other weakly ionic oxides such as the ferroelectric perovskites.[35]

As discussed in Sec. III A, the oxygen atom of type $\mathrm{O}_1$ is bonded to three nearest-neighbor Zr atoms in an almost planar configuration. One might then expect that the largest dynamical charge transfer would occur for motions of the O atom in this plane, with a smaller magnitude of $Z^*$ for motion perpendicular to this plane. To check this, we computed the eigenvectors that result from diagonalizing the symmetric part of the Born charge tensor of the $\mathrm{O}_1$ atom, corresponding to the eigenvalues in the penultimate row of Table IV. Sure enough, the principle axis $\hat{e}_3$ associated with the eigenvalue $Z_3^*=-1.19$ of smallest magnitude points almost directly normal to the plane of the neighbors (making angles of 85°, 91.2°, and 93.9° to the three O-Zr bonds). The other two principal axes lie essentially in the plane of the neighbors, as shown in Fig. 3. Moreover, the principal axis $\hat{e}_1$ connected with the eigenvalue $Z_1^*=-4.26$ of largest magnitude is nearly parallel to the bond to the closest neighbor $\mathrm{Zr}_1$. It can also be seen that the vector $\hat{e}_2$ connected with the intermediate eigenvalue is very nearly aligned with the $\mathrm{O}_1$-$\mathrm{Zr}_3$ bond. Not surprisingly in view of its more tetrahedral coordination, the $\mathbf{Z}^*$ tensor for atom $\mathrm{O}_2$ is more isotropic, as indicated by the smaller spread of the eigenvalues in the last line of Table IV.

### C. Phonons

The frequencies of phonons at $\Gamma$, the center of the Brillouin zone, are calculated for the cubic, tetragonal, and monoclinic phases. For each phase, we first calculate the force-constant matrix

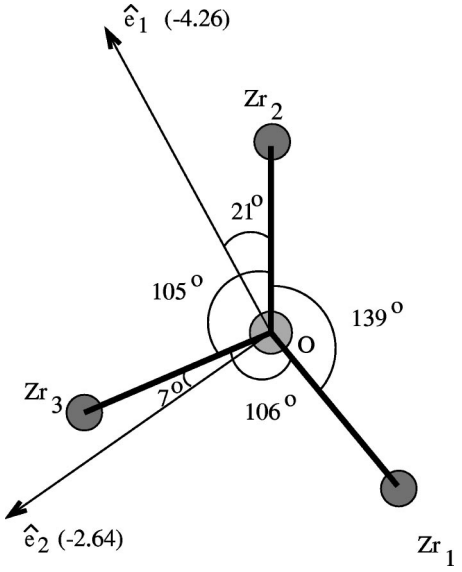


FIG. 3. Environment of threefold-coordinated $\mathrm{O}_1$ atom in the monoclinic phase. The three Zr-O bonds lie approximately in a plane. $\hat{e}_1$ and $\hat{e}_2$ are the two principal axes associated with the eigenvalues $-4.26$ and $-2.64$ of the symmetric part of the $Z^*$ tensor, respectively.

$$\Phi_{ij}^{\alpha\beta}=-\frac{\partial F_i^\alpha}{\partial u_j^\beta}\simeq-\frac{\Delta F_i^\alpha}{\Delta u_j^\beta} \tag{2}$$

obtained by calculating all the Hellmann-Feynman forces ($F_i^\alpha$) caused by displacing each ion in each possible direction ($u_j^\beta$) in turn. (Here Greek indices label the Cartesian coordinates, and $i$ and $j$ run over all the atoms in the unit cell.) In practice, we take steps $\Delta u$ that are 0.2% in lattice units, average over steps in positive and negative directions, and the resulting $\Phi$ matrix is symmetrized to clean up numerical errors. The dynamical matrix $D_{ij}^{\alpha\beta}=(M_iM_j)^{-1/2}\Phi_{ij}^{\alpha\beta}$ is then diagonalized to obtain the eigenvalues $\omega^2$. Once again, we will mainly focus on the monoclinic phase, and briefly summarize the results for the cubic and tetragonal phases.

The low-temperature phase of $\mathrm{ZrO}_2$ is monoclinic, with space group $P2_1/c$. The little group at $\Gamma$ is the point group $C_{2h}$ consisting of operations $E$, $I$, $C_2^y$, and $M_y$. The character table of this point group indicates that there are four symmetry classes and thus four irreducible representations, each of which is one dimensional. A standard group-theoretical analysis indicates that the modes at the $\Gamma$ point can be decomposed as

$$\Gamma_{\mathrm{vib}}^{\mathrm{mono}}=9A_g\oplus 9A_u\oplus 9B_g\oplus 9B_u \tag{3}$$

(see also Ref. 24). Of the 36 modes, 18 modes ($9A_g+9B_g$) are Raman active and 15 modes ($8A_u+7B_u$) are infrared active, the remaining three modes being the zero-frequency translational modes. Only the 15 infrared-active modes contribute to the lattice dielectric tensor, as discussed in the next section. Similarly, for the tetragonal $\mathrm{ZrO}_2$ phase,

TABLE V. Frequencies (in $cm^{-1}$) of IR-active phonon modes for $ZrO_2$ phases. For monoclinic $ZrO_2$, a possible reassignment is proposed. The notation ''sh'' stands for ''shoulder'' as in the original reference. Modes labeled ''weak'' have very small intensity. Reference 37 is a previous theoretical work.

| Cubic | This work | | | |
|---|---|---|---|---|
| 1 | 258($T_{1u}$) | | | |
| Tetrag. | This work | Expt., Ref. 38 | Expt., Ref. 39 | Ref. 37 |
| 1 | 154 ($E_u$) | 140 | 164 | 146 |
| 2 | 437 ($E_u$) | 550 | 467 | 466 |
| 3 | 334 ($A_{2u}$) | 320 | 339 | 274 |
| Mono. | This work | Expt., Ref. 9 | Expt., Ref. 25 | Expt.,Ref. 27 |
| | | 104 | | |
| 1 | 181 ($B_u$)$^{weak}$ | 180 | | |
| | | 192 | | |
| 2 | 224 ($A_u$) | 235 | 220 | 224 |
| 3 | 242 ($A_u$) | | | |
| 4 | 253 ($B_u$) | 270 | 250 | 257 |
| 5 | 305 ($A_u$) | | | |
| 6 | 319 ($B_u$) | | | 324$^{sh}$ (?) |
| 7 | 347 ($A_u$) | | | |
| 8 | 355 ($B_u$) | 360 | 330 | 351 |
| | | 375 | 370 | 376 |
| 9 | 401 ($A_u$) | | | |
| 10 | 414 ($B_u$) | 415 | 420 | 417 |
| | | 445 | 440 | 453$^{sh}$ |
| 11 | 478 ($A_u$) | | | |
| 12 | 483 ($B_u$) | 515 | 520 | 511 |
| 13 | 571 ($A_u$) | 620 | 600 | 588 |
| 14 | 634 ($A_u$)$^{weak}$ | | | 687 (?) |
| | | | | 725 (?) |
| 15 | 711 ($B_u$) | 740 | 740 | 789 |

$$\Gamma_{\text{vib}}^{\text{tetra}} = 1A_{1g} \oplus 2A_{2u} \oplus 3E_g \oplus 3E_u \oplus B_{2u} \oplus 2B_{1g}, \qquad (4)$$

where the $E_u$ and $E_g$ representations are two dimensional while all other modes are one dimensional. One $A_{2u}$ mode and one $E_u$ pair are acoustic, leaving one IR-active $A_{2u}$ and two IR-active $E_u$ pairs; $A_{1g}$, $B_{1g}$, and $E_g$ are Raman active, and $B_{2u}$ is silent (see also Ref. 36). For the cubic phase one finds

$$\Gamma_{\text{vib}}^{\text{cubic}} = 2T_{1u} \oplus T_{1g}, \qquad (5)$$

where both $T_{1u}$ and $T_{1g}$ representations are three dimensional. One of the $T_{1u}$ triplets is translational, leaving one IR-active $T_{1u}$ triplet.

Table V lists our calculated IR-active phonon frequencies in comparison with available theoretical[37] and experimental values.[9,25,27,38,39] In some cases, possible reassignments are suggested. The overall agreement is very good; we obtain all the major features of the experimental infrared spectra. In order to facilitate comparison with experiment, the oscillator strengths of the infrared-active modes [namely, $\epsilon_\lambda$; see Eqs. (8) and (9) of Sec. III D] are calculated and plotted versus frequency in Fig. 4. The horizontal axis is reversed for comparison with experimental spectra such as that of Fig. 2 of Ref. 25. The solid and dashed lines indicate $A_u$ and $B_u$ modes, respectively. The two modes at 181 $cm^{-1}$ and 634 $cm^{-1}$ are very weak, so that it is not surprising that they were not observed in most experiments. The mode at 242 $cm^{-1}$ is buried by the modes at 253 $cm^{-1}$ and 224 $cm^{-1}$, while the mode at 305 $cm^{-1}$ is similarly shadowed by the strongest mode at 319 $cm^{-1}$. Because the pairs of modes at 347/355 $cm^{-1}$, 401/414 $cm^{-1}$, and 478/483 $cm^{-1}$ are very close and of comparable strength, we think that they might be observed as single modes in the experiments.

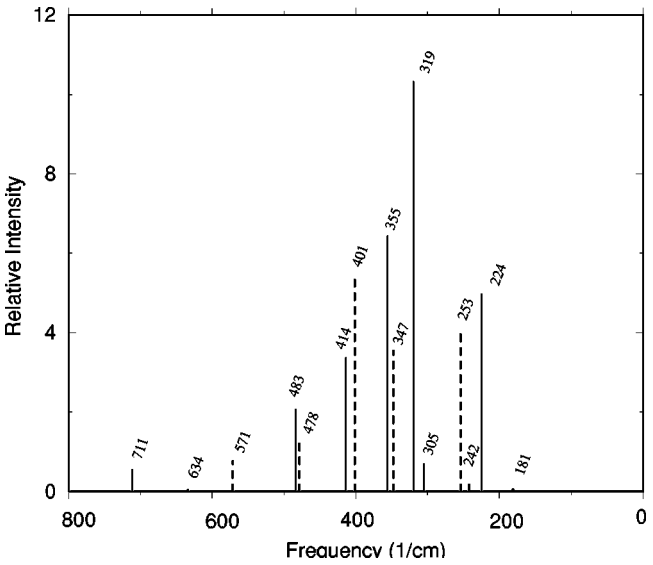


FIG. 4. Calculated spectrum of IR-active modes, in which orientationally averaged intensity [$\epsilon_\lambda$ of Eq. (9)] is plotted vs mode frequency in $cm^{-1}$ (see labels on modes). Solid and dashed lines indicate $A_u$ and $B_u$ IR-active modes, respectively.

The calculated Raman-active phonon mode frequencies for the monoclinic structure are summarized in Table VI. The overall pattern of the calculated Raman-active spectrum agrees quite well with the experimental results, but we again suggest possible reassignments of some of the modes. Specifically, we obtained one Raman-active mode at 180 $cm^{-1}$ that was not observed in either experiment. We agree with Carlone[26] in excluding the mode at 355 $cm^{-1}$ suggested in Ref. 24 and in interpreting the feature at 780 $cm^{-1}$ as a first-order and not a second-order one.[24] On the other hand, our calculations do not give any frequency close to 705 $cm^{-1}$ as observed by Carlone.[26] The mode at 317 $cm^{-1}$ obtained in our calculation is observed somewhat ambiguously in one experiment[24] but not in the other.[26] The reason why we assigned the highest calculated mode at 748 $cm^{-1}$ as shown in Table VI is that the corresponding Raman spectra at 15 K indicated this mode at 745 $cm^{-1}$.[26]

The overall good correspondence between our results and the experimental data for both infrared and Raman-active modes therefore tends to justify our phonon analysis, sug-

TABLE VI. Frequencies ($cm^{-1}$) of Raman-active phonon modes ($A_g$ and $B_g$) in monoclinic $ZrO_2$. Experimental data are measured at 300 K. The assignment connecting the two sets of experimental results is adopted from Ref. 26. We also adopt the notations introduced by the authors of Ref. 24: ''ambig'' for ''observed ambiguously,'' ''tetra'' for ''tetragonal phase,'' ''sugg'' for ''unobserved suggested,'' and ''2nd'' for ''second order.''

| Mode | This work | Mode | Expt., Ref. 26 | Mode | Expt., Ref. 24 |
|---|---|---|---|---|---|
| | | | | 1 | 92 ambig |
| 1 | 103 ($A_g$) | 1 | 99 | 2 | 101 |
| | | | | | 148 tetra |
| 2 | 175 ($B_g$) | 2 | 177 | 3 | 177 |
| 3 | 180 ($A_g$) | | | | |
| 4 | 190 ($A_g$) | 3 | 189 | 4 | 189 |
| 5 | 224 ($B_g$) | 4 | 222 | 5 | 222 |
| | | 5 | 270 | | 266 tetra |
| 6 | 313 ($B_g$) | 6 | 305 | 6 | 306 |
| 7 | 317 ($A_g$) | | | 7 | 315 ambig |
| 8 | 330 ($B_g$) | 7 | 331 | 8 | 335 |
| 9 | 345 ($A_g$) | 8 | 343 | 9 | 347 |
| | | | | 10 | 355 sugg |
| 10 | 381 ($A_g$) | 9 | 376 | | |
| 11 | 382 ($B_g$) | 10 | 376 | 11 | 382 |
| 12 | 466 ($A_g$) | 11 | 473 | 12 | 476 |
| 13 | 489 ($B_g$) | 12 | 498 | 13 | 502 |
| 14 | 533 ($B_g$) | 13 | 534 | 14 | 537 |
| 15 | 548 ($A_g$) | 14 | 557 | 15 | 559 |
| 16 | 601 ($B_g$) | 15 | 613 | 16 | 616 |
| 17 | 631 ($A_g$) | 16 | 633 | 17 | 637 |
| | | 17 | 705 | | |
| 18 | 748 ($B_g$) | 18 | 780 | | 764 2nd |

gesting that we are now on firm ground to proceed to the calculation of the lattice contributions to the dielectric tensors for the $ZrO_2$ phases.

### D. Lattice dielectric tensors

In this section, we present our calculations of the lattice contributions to the static dielectric tensor ($\epsilon_0$), which can be separated into contributions arising from purely electronic screening ($\epsilon_\infty$) and IR-active phonon modes according to[40]

$$\epsilon^0_{\alpha\beta} = \epsilon^\infty_{\alpha\beta} + \frac{4\pi e^2}{M_0 V} \sum_\lambda \frac{\tilde{Z}^*_{\lambda\alpha} \tilde{Z}^*_{\lambda\beta}}{\omega^2_\lambda}. \quad (6)$$

Here $\alpha$ and $\beta$ label Cartesian coordinates, $e$ is the electron charge, $M_0$ is a reference mass that we take for convenience to be 1 amu, $\omega_\lambda$ is the frequency of the $\lambda$th IR-active phonon normal mode, and $V$ is the volume of the 3-atom, 6-atom, or 12-atom unit cell for cubic, tetragonal, or monoclinic cases, respectively. The mode effective charge tensors $\tilde{Z}^*_{\lambda\alpha}$ are given by

TABLE VII. Mode frequency, scalar mode effective charge, and contribution to the trace of the dielectric tensor for each IR-active mode.

| | Mode ($cm^{-1}$) | $\tilde{Z}^*_\lambda$ | $\epsilon_\lambda$ |
|---|---|---|---|
| Cubic | 258 ($T_{1u}$) | 1.17 | 31.80 |
| Tetragonal | 154 ($E_u$) | 1.03 | 34.29 |
| | 334 ($A_{2u}$) | 1.48 | 14.92 |
| | 437 ($E_u$) | 1.35 | 7.27 |
| Monoclinic | 181 ($A_u$) | 0.07 | 0.05 |
| | 224 ($B_u$) | 0.84 | 4.97 |
| | 242 ($A_u$) | 0.22 | 0.31 |
| | 253 ($A_u$) | 0.86 | 4.10 |
| | 305 ($B_u$) | 0.42 | 0.69 |
| | 319 ($B_u$) | 1.72 | 10.33 |
| | 347 ($A_u$) | 1.09 | 3.54 |
| | 355 ($B_u$) | 1.51 | 6.43 |
| | 401 ($A_u$) | 1.57 | 5.44 |
| | 414 ($B_u$) | 1.27 | 3.37 |
| | 478 ($A_u$) | 0.93 | 1.34 |
| | 483 ($B_u$) | 1.16 | 2.07 |
| | 571 ($A_u$) | 0.84 | 0.77 |
| | 634 ($A_u$) | 0.06 | 0.00 |
| | 711 ($B_u$) | 0.88 | 0.55 |

$$\tilde{Z}^*_{\lambda\alpha} = \sum_{i\beta} Z^*_{i,\alpha\beta} \left(\frac{M_0}{M_i}\right)^{1/2} \xi_{i,\lambda\beta}, \quad (7)$$

where $\xi_{i,\lambda\beta}$, the eigendisplacement of atom $i$ in phonon mode $\lambda$, is normalized according to $\Sigma_{i\alpha} \xi_{i,\lambda\alpha} \xi_{i,\lambda'\alpha} = \delta_{\lambda\lambda'}$. It is also convenient to write

$$\mathrm{Tr}[\epsilon^0] = \mathrm{Tr}[\epsilon^\infty] + \sum_\lambda \epsilon_\lambda, \quad (8)$$

where

$$\epsilon_\lambda = \frac{4\pi e^2}{M_0 V \omega^2_\lambda} \tilde{Z}^{*\,2}_\lambda \quad (9)$$

is the contribution to the trace of the dielectric tensor coming from the mode $\lambda$, and the scalar mode effective charge $\tilde{Z}^*_\lambda$ is defined via $\tilde{Z}^{*\,2}_\lambda = \Sigma_\alpha \tilde{Z}^{*\,2}_{\lambda\alpha}$.

Presented in Table VII are the scalar mode effective charges $\tilde{Z}^*_\lambda$ and the corresponding contribution to the static dielectric response $\epsilon_\lambda$ for each IR-active mode. (Note that $T_{1u}$ and $E_u$ modes are threefold and twofold degenerate, respectively. The $\epsilon_\lambda$ vs $\omega_\lambda$ for the monoclinic phase are also presented graphically in Fig. 4.) From Table VII or Fig. 4, we find that for the monoclinic phase the softest modes have small $\tilde{Z}^*_\lambda$ values and hence do not contribute much intensity, while the modes with largest $\tilde{Z}^*_\lambda$ are at significantly higher frequency ($\sim 319$ $cm^{-1}$). This observation will be important for explaining the relative smallness of the dielectric tensor of the monoclinic phase, as discussed below.

When all the modes are summed over, we obtain the total lattice contribution to the static dielectric response [the second term of Eq. (6)]. We find

$$\epsilon^{\rm latt}_{\rm cubic}=\begin{pmatrix} 31.8 & 0 & 0 \\ 0 & 31.8 & 0 \\ 0 & 0 & 31.8 \end{pmatrix},$$

$$\epsilon^{\rm latt}_{\rm tetra}=\begin{pmatrix} 41.6 & 0 & 0 \\ 0 & 41.6 & 0 \\ 0 & 0 & 14.9 \end{pmatrix},$$

$$\epsilon^{\rm latt}_{\rm mono}=\begin{pmatrix} 16.7 & 0 & 0.98 \\ 0 & 15.6 & 0 \\ 0.98 & 0 & 11.7 \end{pmatrix}.$$

The calculated dielectric tensors have the correct forms expected from the crystal point group: the cubic one is diagonal and isotropic, the tetragonal one is diagonal with $\epsilon_{xx}=\epsilon_{yy}\neq\epsilon_{zz}$, and the monoclinic one is only block diagonal in $y$ and $xz$ subspaces. Our values are also in very good agreement with previous theoretical calculations for the cubic and tetragonal phases. Reference 12 reports that $\epsilon^{\rm latt}=29.77$ for the cubic phase, within about 6% of our result. Reference 12 also gives the two independent components of $\epsilon^{\rm latt}$ in the tetragonal phase as 42.36 and 15.03, again in excellent agreement with our results and showing the same enormous anisotropy.

To compare with experiment, we note that $\epsilon_\infty$ can be estimated from the index of refraction $n$, which has been reported experimentally to be about 2.16 ($n^2=\epsilon_\infty=4.67$) (Ref. 11), 2.192 ($\epsilon_\infty=4.805$) (Ref. 10), and 2.19 ($\epsilon_\infty=4.80$) (Ref. 9) for the cubic, tetragonal and monoclinic $ZrO_2$ phases, respectively. Theoretical works have reported that the orientational average $\overline{\epsilon_\infty}=5.75$ for cubic $ZrO_2$ (Ref. 8), and $\epsilon^{\parallel}_\infty=5.28$ and $\epsilon^{\perp}_\infty=5.74$ ($\overline{\epsilon_\infty}=5.59$) for tetragonal $ZrO_2$ (Ref. 12). We can see that $\epsilon_\infty$ does not vary strongly with structural phase; nor is there any evidence for strong anisotropy. Moreover, the only experimental measurements of $\epsilon_0$ of which we are aware are on polycrystalline samples, for which we need to take an orientational average anyway. Therefore, we somewhat arbitrarily assume an isotropic value of $\epsilon_\infty=5.0$ for the purposes of comparison with the total dielectric response. Then we obtain orientationally averaged static dielectric constants of 36.8, 46.6, and 19.7 for the cubic, tetragonal and monoclinic $ZrO_2$ phases, respectively.

Experimental reports of the value of $\epsilon_0$ for monoclinic $ZrO_2$ span a wide range from about 16 to 25 (Refs. 9 and 41); our estimated value of 19.7 falls comfortably in the middle of this range. Unfortunately, we are not aware of any experimental measurements of the static dielectric response in the cubic or tetragonal phase. Since these phases exist only at elevated temperatures, comparison with zero-temperature theory would need to be made with caution in any case. However, neither the cubic-tetragonal nor the tetragonal-monoclinic transition is ferroelectric in character, so the influence of the thermal fluctuations on $\epsilon_0$ is is probably not drastic.

### E. Discussion

As indicated in the Introduction, much current interest in $ZrO_2$ and related oxides is driven by the search for high-$\epsilon_0$ materials for use as the gate dielectric in future-generation integrated-circuit devices. While the dielectric constant of monoclinic $ZrO_2$ is much bigger than that of $SiO_2$, our results indicate that it is actually rather low compared to the values in the range 35–50 expected for the tetragonal and cubic phases. From this perspective, it appears that monoclinic $ZrO_2$ has a disappointingly low static dielectric response.

As can be seen from Eq. (6) or (9), the contribution of a given mode to the dielectric response scales as $\tilde{Z}^{*\,2}_\lambda/\omega^2_\lambda$, so that a large $\epsilon_0$ will result if there are modes that have simultaneously a large $\tilde{Z}^*$ and a small $\omega$. As can be seen from Table VII, this is not the case for monoclinic $ZrO_2$. Instead, we find that the cluster of modes with the lowest frequencies ($<250$ cm$^{-1}$) also have low $\tilde{Z}^*$ values ($<0.5$), while the most active modes reside at higher frequencies ($\sim$ 300–500 cm$^{-1}$). This is in direct contrast to the case of the cubic perovskite $CaTiO_3$ studied recently by Cockayne and Burton,[42] who find a very soft ($\omega\simeq100$ cm$^{-1}$) mode and very active ($\tilde{Z}^*\simeq3$) mode, contributing to an enormous dielectric constant $\epsilon_0>250$.

The much larger values of $\epsilon_0$ obtained for the cubic and tetragonal phases suggests that the unfavorable coincidence of low-$\omega$ and low-$\tilde{Z}^*$ values may be peculiar to the monoclinic phase. Thus, it would be very interesting to explore the effect of other structural modifications (e.g., quasiamorphous structures) on the dielectric response. This clearly presents an avenue for future study.

Finally, in low-symmetry structures such as the monoclinic (or especially amorphous) phases, it is of interest to attempt to decompose $\epsilon_0$ spatially into contributions coming from different atoms in the structure. For example, one might ask whether it is primarily the threefold or fourfold oxygens that are responsible for the dielectric response in the monoclinic phase. For this purpose, we first carry out a decomposition $\epsilon^{\rm latt}_{\alpha\beta}=\Sigma_{ij}\tilde{\epsilon}^{ij}_{\alpha\beta}$ of the lattice dielectric tensor into contributions

$$\tilde{\epsilon}^{ij}_{\alpha\beta}=\frac{4\pi e^2}{V}\sum_\lambda\frac{1}{\kappa_\lambda}R^\lambda_{\alpha i}R^\lambda_{\beta j}$$

arising from pairs of atoms, where $\kappa_\lambda$ and $e^\lambda_{j\beta}$ are the eigenvalue and eigenvector of the force constant matrix $\Phi^{\alpha\beta}_{ij}$ for the phonon mode $\lambda$, $V$ is the volume of unit cell, and $R^\lambda_{\alpha j}=\Sigma_\beta Z^*_{j,\alpha\beta}e^\lambda_{j\beta}$. We then heuristically define the contribution coming from atom $i$ to be

$$\overline{\epsilon}^{(i)}_{\alpha\beta}=\sum_j\frac{1}{2}(\tilde{\epsilon}^{ij}_{\alpha\beta}+\tilde{\epsilon}^{ji}_{\alpha\beta}). \tag{10}$$

This atom-by-atom decomposition attributes most of the contribution to $\epsilon_0$ as coming from the Zr atoms (exactly 2/3 in the cubic phase and close to this ratio in the other two phases). As for the oxygen, we found that both the threefold and fourfold oxygen atoms make a similar contribution to the orientationally averaged dielectric constant in the monoclinic phase. (Not surprisingly, the anisotropies of the two oxygen contributions are somewhat different.) While this analysis has not proved especially fruitful here, it may be useful in future studies of low-symmetry (e.g., amorphous) phases.

## IV. CONCLUSION

In summary, we have investigated here the Born effective charge tensors, lattice dynamics, and the contributions of the lattice modes to the dielectric properties of the three $ZrO_2$ phases. The structural parameters, including all internal degrees of freedom of the three $ZrO_2$ phases, are relaxed, and excellent agreement is achieved with experimental structural refinements and with previous *ab initio* calculations. The observed relative stability of the $ZrO_2$ phases is reproduced in our calculation. The calculated Born effective charge tensors show anomalously large values of $Z^*$, reflecting a strong dynamic charge transfer as the bond length varies and indicating a partially covalent nature of the Zr-O bonds. The calculated zone-center phonon mode frequencies are in good agreement with infrared and Raman experiments.

Finally, the lattice contributions to the dielectric tensors have been obtained. We find that the cubic and tetragonal phases have a much larger static dielectric response than the monoclinic phase, with an especially strong anisotropy in the tetragonal structure. The relatively low $\epsilon_0$ in monoclinic $ZrO_2$ arises because the few lowest-frequency IR-active modes happen to have rather small oscillator strengths, while the modes with the strongest dynamical mode effective charges occur at higher frequency. This result, together with the predicted increase of $\epsilon_0$ in the cubic and tetragonal phases, suggests that the static dielectric constant is a strong function of the structural arrangement. Thus, it may be quite stimulating to investigate the $\epsilon_0$ values in structurally modified (e.g., amorphous) forms of $ZrO_2$, or in solid solutions of $ZrO_2$ with other oxides.

## ACKNOWLEDGMENTS

This work was supported by NSF Grant No. 4-21887. We would like to thank E. Garfunkel for useful discussions. One of us (X.Z.) thanks I. Souza for helpful discussions in connection with the calculation of Born effective charge tensors.

[1] L. C. Feldman, E. P. Gusev, and E. Garfunkel, *Ultrathin Dielectrics in Silicon Microelectrics* (*Fundamental Aspects of Ultrathin Dielectrics on Si-based Devices)*, edited by E. Garfunkel, E. Gusev, and A. Vul (Kluwer Academic, Dodrecht, 1998), p. 39.
[2] D.A. Buchanan and S.H. Lo, Microelectron. Eng. **36**, 13 (1997).
[3] G. Heiser and A. Schenk, J. Appl. Phys. **81**, 7900 (1997).
[4] H.S. Momose, M. Ono, T. Yoshitomi, T. Ohguro, S. I. Nakamura, M. Saito, and H. Iwai, IEEE Trans. Electron Devices **43**, 1233 (1996).
[5] G.B. Alers, D.J. Werder, Y. Chabal, H.C. Lu, E.P. Gusev, E. Garfunkel, T. Gustafsson, and R.S. Urdahl, Appl. Phys. Lett. **73**, 1517 (1998).
[6] J.V. Grahn, P.E. Hellberg, and E Olsson, J. Appl. Phys. **84**, 1632 (1998).
[7] G.D. Wilk, R.M. Wallance, and J.M. Anthony, J. Appl. Phys. **87**, 484 (2000).
[8] F. Detraux, Ph. Ghosez, and X. Gonze, Phys. Rev. Lett. **81**, 3297 (1998).
[9] A. Feinberg and C.H. Perry, J. Phys. Chem. Solids **42**, 513 (1981).
[10] R.H. French, S.J. Glass, F.S. Ohuchi, Y.N. Xu, and W.Y. Ching, Phys. Rev. B **49**, 5133 (1994).
[11] D.L. Wood and K. Nassau, Appl. Opt. **12**, 2978 (1982).
[12] G.-M. Rignanese, F. Detraux, X. Gonze, and A. Pasquarello, Phys. Rev. B **64**, 134301 (2001).
[13] E.V. Stefanovich, A.L. Shluger, and C.R.A. Catlow, Phys. Rev. B **49**, 11 560 (1994).
[14] M. Wilson, U. Schonberger, and M.W. Finnis, Phys. Rev. B **54**, 9147 (1996).
[15] J.K. Dewhurst and J.E. Lowther, Phys. Rev. B **57**, 741 (1998).
[16] B. Králik, E.K. Chang, and S.G. Louie, Phys. Rev. B **57**, 7027 (1998).
[17] G. Jomard, T. Petit, A. Pasturel, L. Magaud, G. Kresse, and J. Hafner, Phys. Rev. B **59**, 4044 (1999).
[18] G. Stapper, M. Bernasconi, N. Nicoloso, and M. Parrinello, Phys. Rev. B **59**, 797 (1999).
[19] S. Fabris, A.T. Paxton, and M.W. Finnis, Phys. Rev. B **61**, 6617 (2000).
[20] H.J.F. Jansen, Phys. Rev. B **43**, 7267 (1991).
[21] C.J. Howard, R.J. Hill, and B.E. Reichert, Acta Crystallogr., Sect. B: Struct. Sci. **44**, 116 (1988).
[22] P. Aldebert and J.P. Traverse, J. Am. Ceram. Soc. **68**, 34 (1985).
[23] R.D. King-Smith and D. Vanderbilt, Phys. Rev. B **47**, 1651 (1993).
[24] E. Anastassakis, B. Papanicolaou, and I.M. Asher, J. Phys. Chem. Solids **36**, 667 (1975).
[25] T. Hirata, Phys. Rev. B **50**, 2874 (1994).
[26] C. Carlone, Phys. Rev. B **45**, 2079 (1992).
[27] H. Zhang, Y. Liu, K. Zhu, G. Siu, Y. Xiong, and C. Xiong, J. Phys.: Condens. Matter **11**, 2035 (1999).
[28] D.M. Ceperley and B.J. Alder, Phys. Rev. Lett. **45**, 566 (1980).
[29] We used the LDA but not the generalized gradient approximation (GGA) in this work for two reasons. First, we wanted to facilitate comparison with previous DFT studies on $ZrO_2$ that were carried out using the LDA. Second, Ref. 17 has tested the effect of the LDA and GGA's (PW91 and PB) on $ZrO_2$. These authors find that while the lattice parameters increase slightly with the use of the GGA ($a$ is augmented less than 1% for the monoclinic $ZrO_2$), the $b/a$ and $c/a$ ratios and internal structural parameters are almost unaffected.
[30] D. Vanderbilt, Phys. Rev. B **41**, 7892 (1990).
[31] H.J. Monkhorst and J.D. Pack, Phys. Rev. B **13**, 5188 (1976).

[32] D.K. Smith and H.W. Newkirk, Acta Crystallogr. **18**, 983 (1965).
[33] R. Ackermann, E.G. Rauh, and C.A. Alexander, High Temp. Sci. **7**, 304 (1975).
[34] R. Resta, M. Posternak, and A. Baldereschi, Phys. Rev. Lett. **70**, 1010 (1993).
[35] W. Zhong, R.D. King-Smith, and D. Vanderbilt, Phys. Rev. Lett. **72**, 3618 (1994).
[36] P. Bouvier, H.C. Gupta, and G. Lucazeau, J. Phys. Chem. Solids **62**, 873 (2001).
[37] A.P. Mirgorodsky, M.B. Smirnov, and P.E. Quintard, J. Phys. Chem. Solids **60**, 985 (1997).
[38] T. Hirata, E. Asari, and M. Kitajima, J. Solid State Chem. **110**, 201 (1994).
[39] C. Pecharromán, M. Ocaña, and C.J. Serna, J. Appl. Phys. **80**, 3479 (1996).
[40] All three $ZrO_2$ phases are nonpiezoelectric, so the fixed-strain and free-stress dielectric tensors are identical for these systems.
[41] G.-M. Rignanese, X. Gonze, and A. Pasquarello, Phys. Rev. B **63**, 104305 (2001).
[42] E. Cockayne and B.P. Burton, Phys. Rev. B **62**, 3735 (2000).